

Observation of tunneling-assisted highly forbidden single-photon transitions in a Ni₄ single-molecule magnet

Yiming Chen,¹ Mohammad D. Ashkezari,^{1,*} Rafael A. Allão Cassaro,^{2,†} Paul M. Lahti,² and Jonathan R. Friedman¹

¹*Department of Physics and Astronomy, Amherst College, Amherst, MA 01002-5000, USA*

²*Department of Chemistry, University of Massachusetts, Amherst, MA 01003, USA*

(Dated: June 11, 2022)

Forbidden transitions between energy levels typically involve violation of selection rules imposed by symmetry and/or conservation laws. A nanomagnet tunneling between up and down states violates angular momentum conservation because of broken rotational symmetry. Here we report observations of highly forbidden transitions between spin states in a Ni₄ single-molecule magnet in which a single photon can induce the spin to change by several times \hbar , nearly reversing the direction of the spin. These observations are understood as tunneling-assisted transitions that lift the standard $\Delta m = \pm 1$ selection rule for single-photon transitions. These transitions are observed at low applied fields, where tunneling is dominated by the molecule's intrinsic anisotropy and the field acts as a perturbation. Such transitions may be exploited in quantum information processing since under certain circumstances decoherence due to fluctuations in local magnetic fields is suppressed.

The last two decades have seen significant advances in the fields of quantum computing and quantum information. Many physical systems have been explored as potential qubits and recent attention to hybrid quantum processors has increased interest in spin systems¹⁻⁴ for use as memory qubits. In particular, molecule-based spin systems⁴⁻⁷ have garnered significant attention because of the possibility to chemically engineer the spin's environment to tune spin-anisotropy parameters, coupling to decohering degrees of freedom, etc. Single-molecule magnets (SMMs) are a subclass of these molecular spin systems that typically have large spin and slow magnetic relaxation rates due to the existence of an energy barrier between spin-orientation states. They have been extensively studied⁸ and have been proposed as potential candidates for qubits⁹ and high-density quantum memories.¹⁰

SMMs typically have significant anisotropy that breaks the zero-field degeneracy of magnetic sublevels. They also exhibit remarkable quantum dynamics including quantum tunneling of magnetization (QTM)¹¹ and quantum-phase interference¹². Decoherence is a major obstacle in the implementation of any qubit. For spin systems, decoherence arises from dipolar and hyperfine interactions, electromagnetic field noise, etc. These sources of decoherence can variously be addressed by dilution or separation of the spins to reduce dipole coupling or the use of isotopic substitution to minimize hyperfine interactions, among other techniques.^{5,7,13,14} From a quantum coherence perspective, forbidden transitions have some distinct advantages. Since the matrix elements for these transitions are small, they tend to have long lifetimes. Furthermore, forbidden transitions can be less susceptible to magnetic-field fluctuations under certain circumstances, potentially leading to longer coherence times.^{3,15} Here we investigate highly forbidden transitions between magnetic sublevels in an SMM at low applied fields, where the relevant matrix elements are only weakly perturbed by the external field. We observe forbidden tran-

sitions in which there is a large change in the value of the magnetic quantum number m while the transition matrix element is dominated by the molecule's intrinsic anisotropy rather than by an external field.

We studied the $S = 4$ complex [Ni(hmp)(dmb)Cl]₄, (hereafter Ni₄), shown in the inset of Fig. 1. The molecule has large ligands that serve to isolate the Ni₄ magnetic centers within a crystal from each other.¹⁶ In addition, there are no solvate molecules in the crystal lattice and 99% (natural abundance) of Ni nuclei have spin $I = 0$. This SMM has been characterized by electron-spin resonance (ESR) spectroscopy,¹⁷⁻²² magnetization measurements^{16,18,23} and heat capacity measurements.^{21,24,25} Ni₄ can be well described as a single "giant spin" with the Hamiltonian:²²

$$H = -DS_z^2 + BS_z^4 + C(S_+^4 + S_-^4) + \mu_B \vec{B} \cdot \mathbf{g} \cdot \vec{S}, \quad (1)$$

where g is the molecule's g factor, D and B are axial anisotropy parameters responsible for making the lowest energy states be those with the spin parallel or antiparallel ($m = \pm 4$) with the z axis and producing an energy barrier between those two orientations, and C is a transverse anisotropy parameter that affects the strength of tunneling through the barrier. A dc magnetic field applied along the easy (z) axis changes the energies of the magnetic sublevels, as illustrated in Fig. 1. When levels cross, tunneling between them can occur because the off-diagonal terms in Eq. 1 (third term and Zeeman interaction with a transverse field component \vec{B}_T (perpendicular to z)) mix states of different m values. Since these terms do not commute with S_z , they are responsible for the observed tunneling phenomena in this and other SMMs.^{8,11} The off-diagonal terms give rise to avoided level crossings; the energy splitting at an avoided crossing is often dubbed the "tunnel splitting".

In our experiments, tunneling permits a violation of the standard single-photon-transition selection rule $\Delta m = \pm 1$, enabling the observation of highly forbidden transitions. These kinds of forbidden transitions have

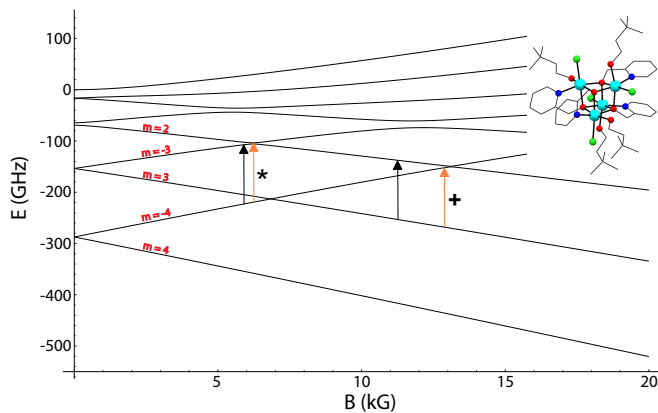


FIG. 1. Spin-state energy-level diagram for Ni_4 . Energies of various levels are shown as a function of magnetic field, calculated by diagonalizing the molecule’s spin Hamiltonian. The diagram illustrates the levels’ behavior when $\theta = 30^\circ$. Arrows indicate the major transitions observed in this study: Black = allowed, orange = forbidden. The two orange arrows are labeled with \star and $+$, the designations used throughout this article. Inset: Molecular unit of $[\text{Ni}(\text{hmp})(\text{dmb})\text{Cl}]_4$ (Ref. 16), where hmp is the anion of 2-hydroxymethylpyridine and dmb is 3,3-dimethyl-1-butanol. Color code: green: chloride; cyan: nickel(II); black: carbon; red: oxygen; blue: nitrogen. Hydrogen atoms are omitted for clarity.

been observed in some SMMs: a mononuclear holmium complex with a large transverse anisotropy term¹⁴ and in Ni_4 when a large B_T was applied to create a large tunnel splitting between the ground states near zero field, creating states that are superpositions of m states.¹⁸ In contrast to the latter work, our experiments involve the application of much smaller values of B_T in which the tunnel splitting is dominated by the SMM’s intrinsic anisotropy and the field acts as a perturbation. In a typical ESR experiment, the Zeeman interaction is the dominant energy as a result of a large applied field. Our experiments, however, lie in the low-Zeeman-energy regime, allowing the observation of transitions between levels localized on opposite sides of the energy barrier. These observations allow a direct probe of transverse anisotropy and provide a platform for investigating decoherence mechanisms of tunneling phenomena.

Samples of Ni_4 were produced using published procedures.²³ Single crystals of typical dimension ~ 1 mm were produced and crystal structure verified through unit cell parameters using X-ray diffractometry. We performed reflection ESR spectroscopy using a custom-built experimental probe within a Quantum Design PPMS. ESR measurements utilized the TE_{011} resonant mode of a 3-D cylindrical cavity with frequency of ~ 115.54 GHz at low temperature and a quality factor (Q) of ~ 8000 . A static magnetic field \vec{H} was applied along the axis of the cavity. A single crystal of Ni_4 was mounted onto the bottom of the cavity with grease. The rf field at the sample position was along the radius of the cavity, perpendicular to the static field. The easy

axis of the crystal was manually tilted at various angles (θ_H) relative to the static field, \vec{H} . We measured the reflected power as a function of frequency, recording the dependence with an oscilloscope, and then extracting the cavity-spin resonant frequency and Q value.

Figure 2 shows ESR spectra (Q vs. H) at 1.8 K for an aligned single crystal of Ni_4 at multiple values of θ_H , the angle between the easy axis and \vec{H} . For many values of θ_H (e.g. 36.4°), we observe multiple resonance peaks: two large peaks that are each split, often with small peaks on the right or left of the large peaks or on their shoulders. Dispersive spectra show corresponding features.²⁶ The large peaks are due to allowed transitions with $\Delta m \simeq \pm 1$. The splitting of the allowed peaks arises from ligand conformational disorder.²⁴ The additional fine structure that some of the split peaks exhibit²¹ is not relevant to this study. We focus on the two small side peaks (marked \star and $+$ in Fig. 2) that we identify as forbidden transitions corresponding roughly to $m = -4 \rightarrow m = 2$ (\star) and $m = 3 \rightarrow m = -4$ ($+$) (cf. orange arrows in Fig. 1). Compared with the allowed transitions, these forbidden transitions have markedly different dependencies on θ_H , confirming the different nature of the transitions. Figure 3 shows the $B - \theta$ resonance positions (determined from the spectra in Fig. 2), where θ is the angle between the easy axis and the field \vec{B} experienced by the molecules. The lines in the figure show the calculated resonance points for the transitions shown in Fig. 1, obtained by diagonalizing Eq. 1 using the parameters given below. Allowed (forbidden) transitions are shown using solid (dashed) curves.

The agreement between the calculated $B - \theta$ resonance positions and the experimental data is very good. In producing Fig. 3, we took into account that both the magnitude and direction of \vec{B} changes with \vec{H} due to intermolecular dipolar interactions, so that each spectrum in Fig. 2 produces a range of θ values in Fig. 3 (see Ref. 26). The red and black curves in the figure are the predicted resonance positions for the two conformational states of the molecule, which have somewhat different anisotropy constants, determined by fitting (see Ref. 26): $D = 15.35(1)$ GHz, $B = 0.1282(2)$ GHz and $C = 0(3)$ MHz (red), and $D = 16.627(5)$ GHz, $B = 5.2(3)$ MHz, $C = 5.2(7)$ MHz, and $A = 4.82(2)$ MHz (black), where for the “black” component we found it necessary to include a sixth-order axial anisotropy term, AS_z^6 . Both components were taken to have identical g factors: $g_z = 2.3$ and $g_x = g_y = 2.23$. We found that ϕ , the angle between \vec{B}_T and the spin’s hard (x) axis direction, has negligible effect on the simulated spectra and we simply set it at $\phi = 0^\circ$. Because spectra for the “black” component include allowed transitions in both wells and forbidden transitions near avoided level crossings, the fitting is extremely sensitive to the anisotropy-parameter values and a satisfactory fit cannot be found without including the sixth-order term. The red component has less stringent constraints – its lower-field (\star) forbidden transition is not

observable – and the sixth-order term is not required for a good fit, although that does not obviate its existence; little information can be determined about tunneling for this component, as seen by the large uncertainty in its value of C . The value of A for the “black” component is surprisingly large and supports the conclusion that the giant-spin approximation is not robust in this system because of the relatively weak exchange coupling between Ni ions within the molecule.^{27,28} Nevertheless, the $S = 4$ spin manifold is still well isolated from higher manifolds at low fields, making an effective giant-spin model a viable approximation for the purposes of our analysis.

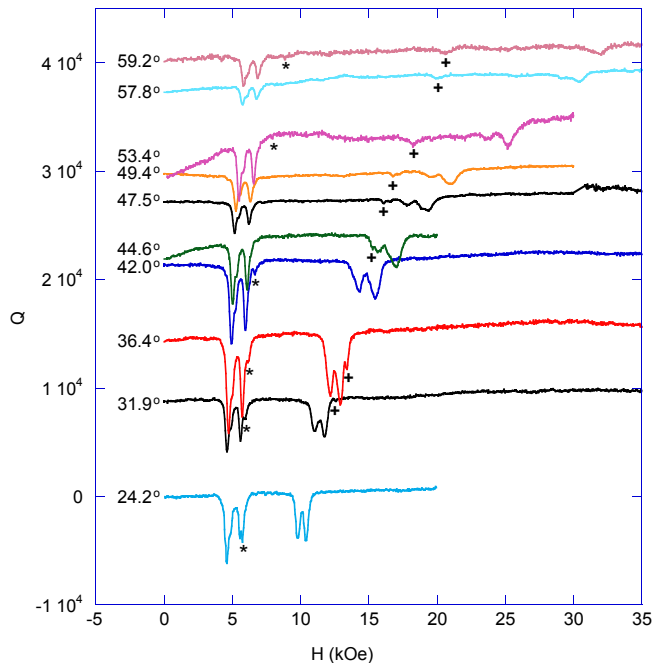


FIG. 2. ESR spectra at 1.8 K for several angles θ_H , the angle between the crystal’s easy axis and the applied field \vec{H} . Spectra were obtained by measuring the cavity-sample resonance to determine resonant frequency and quality factor Q . In this figure, Q is plotted as a function of H . The spectrum for $\theta_{H,ref} = 31.9^\circ$ shows actual Q values. All other spectra have been shifted vertically by an amount proportional to $\theta_H - \theta_{H,ref}$. Spectra from three different crystals are combined in this figure. Each spectrum has been shifted slightly horizontally to account for inductive effects due to sweeping H (see Ref. 26).

To understand how tunneling makes the forbidden transitions observable, we note that each forbidden transition (orange arrows in Fig. 1) occurs at a field near an avoided level crossing, at which resonant tunneling takes place. Tunneling effects can be demonstrated by expanding the two energy eigenstates associated with each forbidden transition in the eigenbasis of S_z

$$|E_j\rangle = \sum_m c_m^{(j)} |m\rangle, \quad (2)$$

where $c_m^{(j)} = \langle m|E_j\rangle$ are probability amplitudes associ-

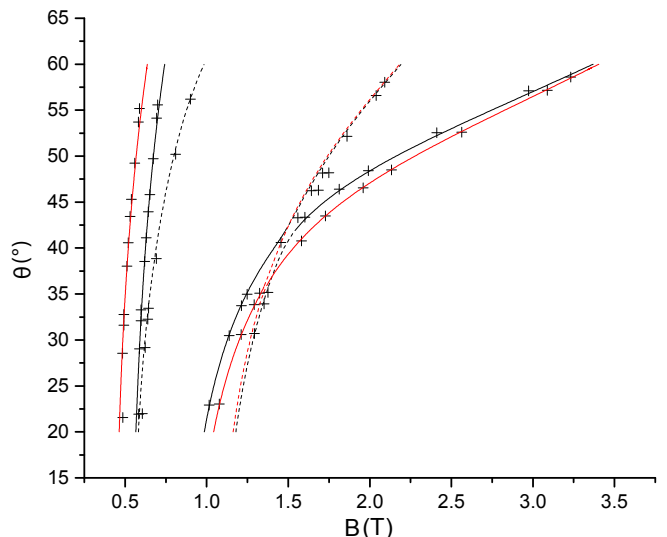


FIG. 3. Resonance field B as a function of θ . The points are the peak positions from Fig. 2 after correcting for the effects of dipole fields (see Ref. 26). The lines are the results of simulations after fitting the observed spectra. Black and red correspond to different conformational states of the molecule with correspondingly different anisotropy constants. Solid curves indicate allowed transitions and dashed curves correspond to forbidden transitions.

ated with projecting the energy eigenstate E_j into the basis of $|m\rangle$ states. Figures 4(a) and 4(b) show the values of $c_m^{(i)}$ as a function of m for the two states involved in the \star and $+$ forbidden transitions, respectively, at $\theta = 30^\circ$. For \star , the initial state is $|i\rangle \approx |m = -4\rangle$, while the final state $|f\rangle$ is a superposition of primarily $|m = 2\rangle$, $|m = -3\rangle$, and $|m = 1\rangle$. The proximity of the resonant field to the field associated with tunneling leads to a small amplitude of $|m = -3\rangle$ in $|f\rangle$, giving rise to a $\Delta m = 1$ transition matrix element between the two energy eigenstates. Thus, the transition between states largely localized in separate wells can be viewed as a tunneling-assisted forbidden transition. Were the photon resonance (orange arrow in Fig. 1) to occur far from the avoided crossing, the forbidden transitions would be suppressed. Equivalently, the forbidden transition can be viewed as tunneling from a single-photon dressed state $|i\rangle \approx |m = -4, n = 1\rangle$ state into the $|f\rangle \approx |m = 2, n = 0\rangle$ state, where n indicates photon number. During this forbidden transition, the change of m is nominally 6; a more rigorous calculation using the parameters for the “black” component yields a change in expectation value $\langle S_z \rangle$ as large as 5, as shown in Fig. 5 (green), indicating a large change in the spin’s angular momentum with the absorption of a single photon.

A similar analysis can be made for the $+$ transition (Fig. 4(b)), where the transition is associated with $|i\rangle \approx |m = 3\rangle$ and $|f\rangle$, a superposition of mostly the $|m = -4\rangle$, $|m = -3\rangle$ and $|m = 2\rangle$ states. Once again, the transition is enabled by the fact that the resonance

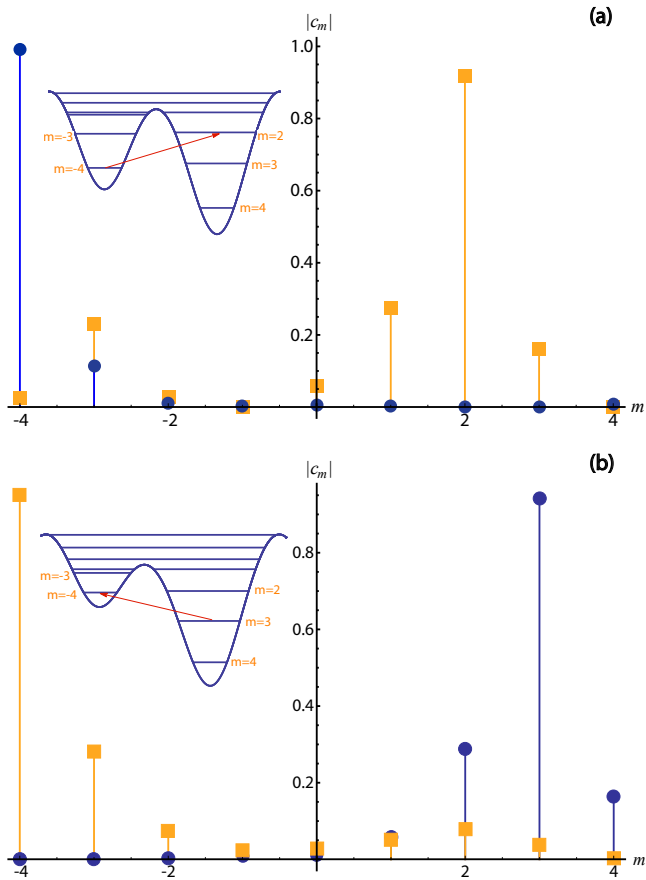


FIG. 4. Decomposition of spin states involved in the forbidden transitions in the m basis (cf. Eq.(2)). Values of c_m were calculated by diagonalizing the spin Hamiltonian at the fields corresponding to the (a) \star and (b) $+$ transitions, setting $\theta = 30^\circ$. Blue circles (orange squares) indicate the values of $|c_m|$ for the lower (upper) state involved in each transition. Insets schematically show the double-well potentials for the associated transitions, marked with red arrows.

field is close to a tunneling field, leading to a small, but appreciable amplitude of the $|m = 2\rangle$ state in $|f\rangle$. The calculation of the change in $\langle S_z \rangle$ (Fig. 5 – blue) indicates a value as high as ~ 7 for the values of θ used in our experiments. $\langle S_z \rangle$ is suppressed at $\theta \sim 20^\circ$ for \star and $\theta \sim 42^\circ$ for $+$ due to the fact that near these angles, the corresponding transitions take place very close to an avoided level crossing, delocalizing the states (e.g. the amplitude of $\langle m = 2 | f \rangle$ for $+$ becomes substantial). We also see that for $\theta \gtrsim 50^\circ$, $\Delta \langle S_z \rangle$ for both transitions decreases because the tunnel splitting is getting larger with increasing θ and, hence, $|i\rangle$ and $|f\rangle$ each contain larger contributions from several $|m\rangle$ states.

As can be seen in Fig. 2, the peaks associated with the forbidden transitions are stronger when they are close to the allowed transitions, confirming the delocalization of $|f\rangle$ near the tunneling resonance field. To quantify this observation, we determine the spectral intensity of each peak in each spectrum by measuring the total area of

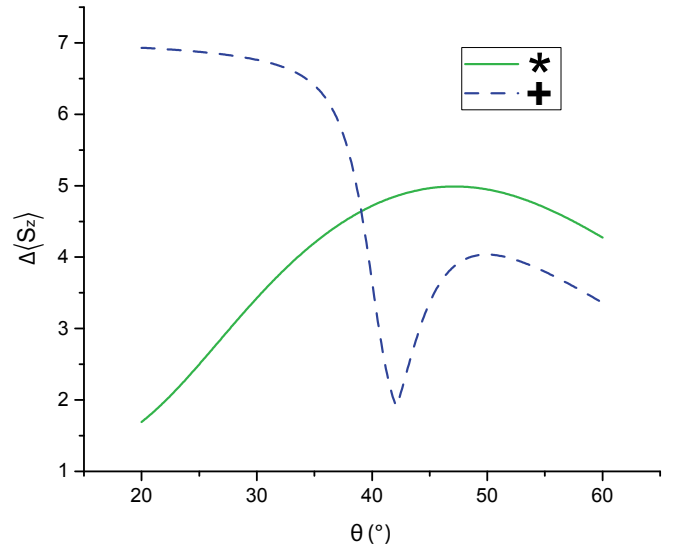


FIG. 5. Calculated $\Delta \langle S_z \rangle$ as a function of θ for the two forbidden transitions studied. Each curve has a dip at the value of θ where the forbidden transitions take place near an avoided level crossing.

the peak after subtracting background. We compared this with the calculated transition intensity $|\langle f | S_T | i \rangle|^2$, where $S_T = \vec{S} \cdot \hat{B}_{rf}$. We normalized each quantity so the total intensity for all transitions in a given spectrum is unity. Figures 6(a) and 6(b) shows a comparison of the experimental (points) and simulated (curves) spectral intensity of the \star and $+$ forbidden transitions, respectively, as a function of θ . Figure 6(a) contains the \star transition intensity for the “black” component only since the corresponding transition for the “red” component is too weak to be observed. For the $+$ transition, the peaks from the two components overlap (c.f. Fig. 3) and cannot be easily distinguished. So, Fig. 6(b) shows the combined intensity for both components. Both panels show good agreement (excepting for $\theta > 50^\circ$ in Fig. 6(b)) between experiment and simulation, with the intensity growing near avoided crossings or at large transverse fields (large angles in Fig. 6(b)), where tunneling is enhanced.

Another interesting feature of the spectra in Fig. 2 is that the linewidths of the peaks associated with forbidden transitions tend to be significantly smaller than for the allowed transitions. This suggests that these peaks are homogeneously broadened. Inhomogeneous broadening due to a distribution of dipolar fields would produce peaks of nearly the same width. On the other hand, homogeneously broadened lines should have a width that scales as $1/\Delta \langle S_z \rangle$, an effect we find roughly borne out by our data. Figure 7 shows values of the decoherence time T_2 extracted from the measured linewidths as a function of θ for the four transitions (two allowed and two forbidden) examined in this study. To obtain T_2 , we fit the peaks in each spectra in Fig. 2 to Lorentzians to determine the width ΔH (in Oersted). After converting

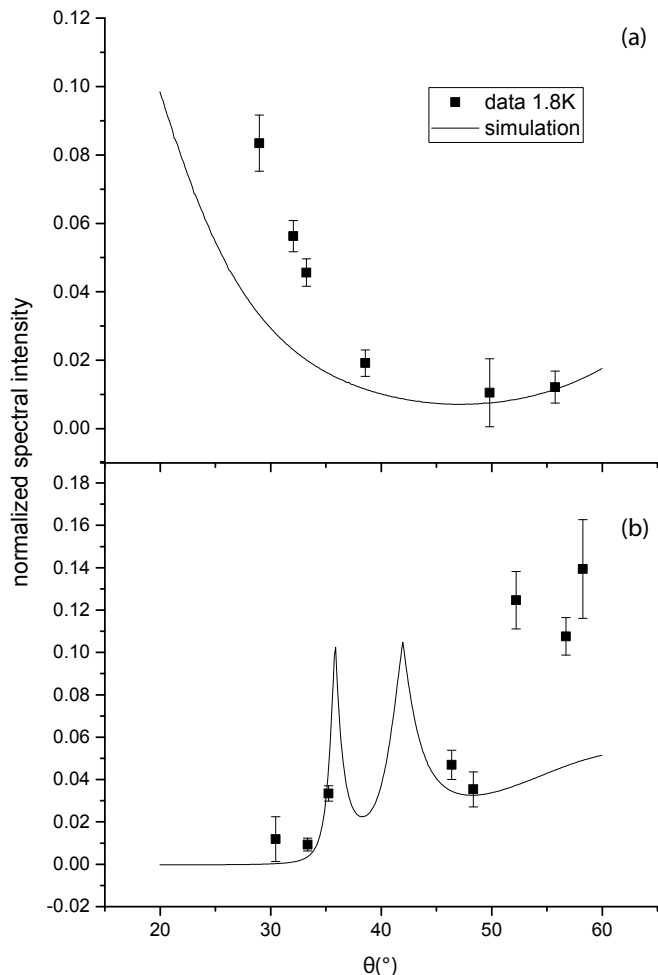


FIG. 6. Spectral intensity as a function of θ for the (a) \star and (b) $+$ forbidden transitions. Points are experimental data determined from the area of the associated peaks. Curves are simulation results based on calculated transition matrix elements, as described in the main text. For (a), the data and simulations are for the “black” transitions only. In contrast, because the peaks for $+$ transitions substantially overlap, the experimental and calculated data in (b) represent the combined intensity for both components.

to a width ΔB (in Gauss), we used the calculated field dependence of the transition frequency, $\partial f/\partial B$ to determine $T_2 = (\frac{\partial f}{\partial B} \frac{\partial B}{\partial H} \Delta H)^{-1}$. The analysis was done for the peaks associated with the “black” component (cf. Fig. 3). While there is some systematic dependence of T_2 on θ and a few anomalous points, the data are consistent with $T_2 \approx 1$ ns. This is comparable but somewhat longer than T_2 measurements reported earlier for this molecule.¹⁸ Long T_2 times have been achieved in a variety of molecular spin systems by various methods of dilution^{4,5,13} to reduce dipole couplings and a similar approach may be possible with Ni_4 by cocrystallizing it with the diamagnetic analog Zn_4 . Even in the absence of such techniques, the short T_2 found in this study may be compensated by the high density of Ni_4 molecules in a crystal that leads

to an enhanced coupling to the radiation field.²⁹

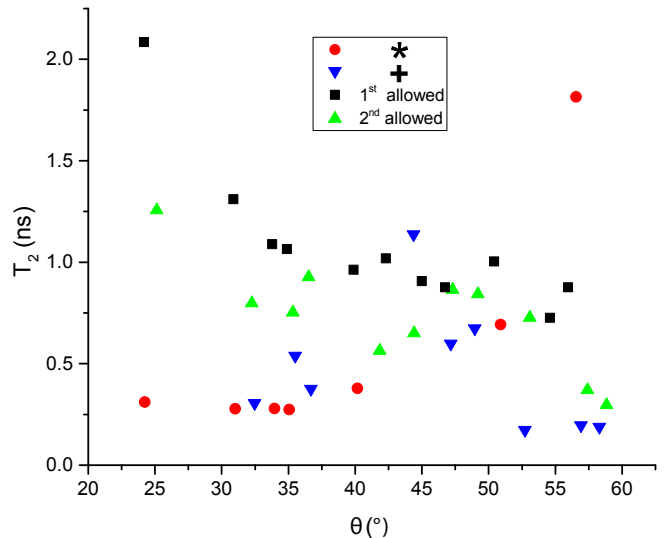


FIG. 7. Decoherence time T_2 for allowed and forbidden transitions, as indicated, as a function of θ . Data were extracted from peak widths of spectra in Fig. 2. Most of the data presented are for the “black” component only. For the $+$ transition, the peaks for the two components overlap at most values of θ and cannot be distinguished. Under those circumstances, T_2 values for that transition represent the width of the combined peak for both components.

The mechanisms of decoherence cannot be unambiguously determined in the present study. We do observe that linewidths tend to increase with increasing temperature.²⁶ This may correspond to a reduced lifetime of the excited states due to higher acoustic-phonon populations at higher temperature. Alternatively, larger dipole and hyperfine field fluctuations at increased temperature may promote decoherence since typically the Zeeman effect causes the states’ energies to vary linearly with field. One way to circumvent this issue is to operate at a field near an avoided crossing where $\partial f/\partial B = 0$ such that the field fluctuations can only affect energies quadratically. Such working points are routinely used in atomic clocks¹⁵ and superconducting qubits³⁰, and have recently been investigated in Bi-doped Si (Ref. 3). The forbidden transitions observed in our study are near such “clock transitions”. Our results for Ni_4 suggest the possibility of operating at these points, permitting an investigation of whether decoherence due to field fluctuations can be suppressed at these transitions.

We compare our work to measurements of photon-assisted tunneling in the Fe_8 SMM³¹. There the ESR resonance field and the tunneling field coincide and the process can be interpreted as an allowed ESR transition followed sequentially by tunneling between wells. In contrast, in our experiments the observed forbidden transitions lie slightly away from tunneling fields, permitting *direct* single-photon transitions between states largely localized in opposite wells. Since tunnel splittings are much

stronger in Ni_4 ($\sim 1 - 2$ GHz for the avoided crossings studied herein) than in Fe_8 (\sim kHz), tunneling effects can be observed when B is somewhat detuned from the tunneling resonance, allowing simultaneous probing of both pairs of levels involved in the avoided crossing.

ACKNOWLEDGMENTS

We are indebted to C. Collett and M. P. Sarachik for useful discussions and comments on the manuscript. We are grateful to H. Xu for her assistance in some aspects of the numerical simulations. We thank C. Euvrard (Millitech Corp.) for technical help with some equipment, J. Kubasek for assistance in fabrication of the resonator and N. Page for technical support of measurement equipment. Support for this work was provided by the U.S. National Science Foundation under Grant No. DMR-1310135, and by the Amherst College Dean of Faculty. R.A.A.C. thanks CNPq for the fellowship that enabled his work at the University of Massachusetts Amherst.

-
- * Current address: Department of Earth, Atmospheric and Planetary Sciences, Massachusetts Institute of Technology, Cambridge, Massachusetts 02139, USA
- † Current address: Instituto de Química, Universidade do Rio de Janeiro, Rio de Janeiro, RJ, 21945-970 Brazil
- ¹ D. I. Schuster, A. P. Sears, E. Ginossar, L. DiCarlo, L. Frunzio, J. J. L. Morton, H. Wu, G. A. D. Briggs, B. B. Buckley, D. D. Awschalom, and R. J. Schoelkopf, *Phys. Rev. Lett.* **105**, 140501 (2010).
 - ² Y. Kubo, F. R. Ong, P. Bertet, D. Vion, V. Jacques, D. Zheng, A. Dréau, J.-F. Roch, A. Auffeves, F. Jelezko, J. Wrachtrup, M. F. Barthe, P. Bergonzo, and D. Esteve, *Phys. Rev. Lett.* **105**, 140502 (2010).
 - ³ G. Wolfowicz, A. M. Tyryshkin, R. E. George, H. Riemann, N. V. Abrosimov, P. Becker, H.-J. Pohl, M. L. W. Thewalt, S. A. Lyon, and J. J. L. Morton, *Nat Nano* **8**, 561 (2013).
 - ⁴ K. Bader, D. Dengler, S. Lenz, B. Endeward, S.-D. Jiang, P. Neugebauer, and J. van Slageren, *Nat Commun* **5**, 6304 (2014).
 - ⁵ A. Ardavan, O. Rival, J. J. L. Morton, S. J. Blundell, A. M. Tyryshkin, G. A. Timco, and R. E. P. Winpenny, *Phys. Rev. Lett.* **98**, 057201 (2007).
 - ⁶ L. Bogani and W. Wernsdorfer, *Nat Mater* **7**, 179 (2008).
 - ⁷ C. J. Wedge, G. A. Timco, E. T. Spielberg, R. E. George, F. Tuna, S. Rigby, E. J. L. McInnes, R. E. P. Winpenny, S. J. Blundell, and A. Ardavan, *Phys. Rev. Lett.* **108**, 107204 (2012).
 - ⁸ J. R. Friedman and M. P. Sarachik, *Annual Review of Condensed Matter Physics* **1**, 109 (2010).
 - ⁹ M. N. Leuenberger and D. Loss, *Nature* **410**, 789 (2001).
 - ¹⁰ R. Sessoli, D. Gatteschi, A. Caneschi, and M. A. Novak, *Nature* **365**, 141 (1993).
 - ¹¹ J. R. Friedman, M. P. Sarachik, J. Tejada, and R. Ziolo, *Physical review letters* **76**, 3830 (1996).
 - ¹² W. Wernsdorfer and R. Sessoli, *Science* **284**, 133 (1999).
 - ¹³ C. Schlegel, J. van Slageren, M. Manoli, E. K. Brechin, and M. Dressel, *Phys. Rev. Lett.* **101**, 147203 (2008).
 - ¹⁴ S. Ghosh, S. Datta, L. Friend, S. Cardona-Serra, A. Gaita-Ariño, E. Coronado, and S. Hill, *Dalton Trans.* **41**, 13697 (2012).
 - ¹⁵ J. J. Bollinger, J. D. Prestage, W. M. Itano, and D. J. Wineland, *Phys. Rev. Lett.* **54**, 1000 (1985).
 - ¹⁶ E.-C. Yang, W. Wernsdorfer, S. Hill, R. S. Edwards, M. Nakano, S. Maccagnano, L. N. Zakharov, A. L. Rheingold, G. Christou, and D. N. Hendrickson, *Polyhedron* **22**, 1727 (2003).
 - ¹⁷ R. S. Edwards, S. Maccagnano, E.-C. Yang, S. Hill, W. Wernsdorfer, D. Hendrickson, and G. Christou, *Journal of Applied Physics* **93**, 7807 (2003).
 - ¹⁸ E. del Barco, A. D. Kent, E. C. Yang, and D. N. Hendrickson, *Phys. Rev. Lett.* **93**, 157202 (2004).
 - ¹⁹ G. de Loubens, G. D. Chaves-O'Flynn, A. D. Kent, C. Ramsey, E. d. Barco, C. Beedle, and D. N. Hendrickson, *Journal of Applied Physics* **101**, 09E104 (2007).
 - ²⁰ G. de Loubens, A. D. Kent, V. Krymov, G. J. Gerfen, C. C. Beedle, and D. N. Hendrickson, *Journal of Applied Physics* **103**, 07B910 (2008).
 - ²¹ J. Lawrence, E.-C. Yang, R. Edwards, M. M. Olmstead, C. Ramsey, N. S. Dalal, P. K. Gantzel, S. Hill, and D. N. Hendrickson, *Inorg. Chem.* **47**, 1965 (2008).
 - ²² J. Lawrence, E.-C. Yang, D. N. Hendrickson, and S. Hill, *Physical Chemistry Chemical Physics* **11**, 6743 (2009).
 - ²³ E.-C. Yang, W. Wernsdorfer, L. N. Zakharov, Y. Karaki, A. Yamaguchi, R. M. Isidro, G.-D. Lu, S. A. Wilson, A. L. Rheingold, H. Ishimoto, and D. N. Hendrickson, *Inorg. Chem.* **45**, 529 (2006).
 - ²⁴ D. N. Hendrickson, E.-C. Yang, R. M. Isidro, C. Kirman, J. Lawrence, R. S. Edwards, S. Hill, A. Yamaguchi, H. Ishimoto, W. Wernsdorfer, C. Ramsey, N. Dalal, and M. M. Olmstead, *Polyhedron Proceedings of the 9th International Conference on Molecule-based Magnets (ICMM 2004) 9th International Conference on Molecule-based Magnets*, **24**, 2280 (2005).
 - ²⁵ C. C. Beedle, J. J. Henderson, P.-C. Ho, T. Sayles, M. Nakano, J. R. O'Brien, K. J. Heroux, E. del Barco, M. B. Maple, and D. N. Hendrickson, *Inorg. Chem.* **49**, 5780 (2010).
 - ²⁶ See supplemental material at [URL will be inserted] for experimental methods, additional data and details of data-analysis techniques.
 - ²⁷ A. Wilson, J. Lawrence, E.-C. Yang, M. Nakano, D. N. Hendrickson, and S. Hill, *Phys. Rev. B* **74**, 140403 (2006).
 - ²⁸ J. Liu and S. Hill, *Polyhedron ICMM 2012*, **66**, 147 (2013).
 - ²⁹ A. Eddins, C. Beedle, D. Hendrickson, and J. R. Friedman, *Phys. Rev. Lett.* **112**, 120501 (2014).
 - ³⁰ D. Vion, A. Aassime, A. Cottet, P. Joyez, H. Pothier,

C. Urbina, D. Esteve, and M. H. Devoret, *Science* **296**, 886 (2002).

- ³¹ L. Sorace, W. Wernsdorfer, C. Thirion, A.-L. Barra, M. Pacchioni, D. Mailly, and B. Barbara, *Phys. Rev. B* **68**, 220407 (2003).

Supplementary Information for Observation of tunneling-assisted highly forbidden single-photon transitions in a Ni₄ single-molecule magnet

Yiming Chen,¹ Mohammad D. Ashkezari,¹ Rafael A. Allão Cassaro,² Paul M. Lahti,² and Jonathan R. Friedman¹

¹Department of Physics and Astronomy, Amherst College, Amherst, MA 01002-5000, USA

²Department of Chemistry, University of Massachusetts, Amherst, MA 01003, USA

(Dated: October 11, 2015)

I. MEASUREMENT APPARATUS AND PROCEDURE

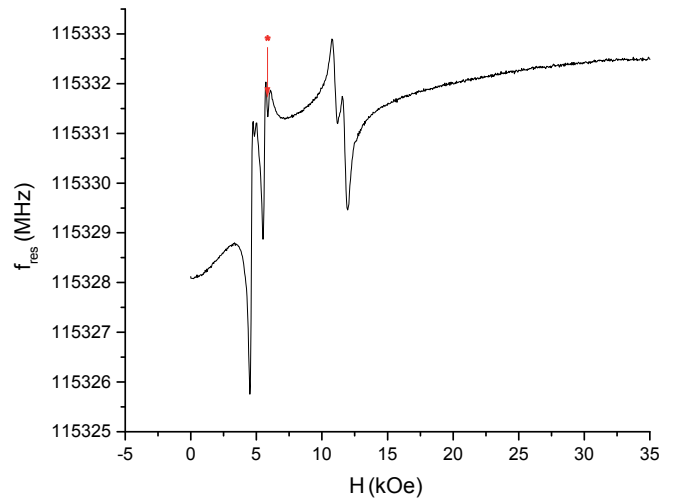
An Agilent 83650B signal generator was used as microwave source. A combination of a 4X active multiplier and a passive doubler was employed to cover the operational frequency range of 100-150 GHz. The resulting microwave signal was injected into a resonant cavity via an approximately a \sim 1-m-long WR-10 waveguide (gold-plated stainless steel with \sim 3 dB insertion loss). The cavity is located in the sample chamber of the apparatus at cryogenic temperatures. Power was controlled with an adjustable attenuator at the room-temperature end of the waveguide. A phase shifter was used to control the frequency of waveguide resonances (by changing the effective length of the waveguide) to mitigate their influence on the cavity resonance. Reflected power was monitored using a directional coupler and a diode detector.

The 3-D cylindrical resonant cavity was machined out of oxygen-free copper (cavity dimensions: diameter = 3.38 mm, depth = 6.86 mm). ESR measurements utilized the cavity's TE₀₁₁ resonant mode with resonant frequency of \sim 115.54 GHz. A small quartz rod was placed along the axis of the cavity to break the degeneracy of the TE₀₁₁ and TM₁₁₁ modes. The cavity was coupled to the end of the waveguide through a 0.76-mm-thick copper coupling plate with a center coupling hole of diameter 0.64 mm. We measured the reflected power as a function of frequency. After subtraction of a smooth frequency-dependent background signal (primarily due to waveguide resonances), a Lorentzian fit is applied to extract the resonance frequency and Q value of the cavity at each field, resulting in one data point on the dispersive spectrum (Supplementary Fig. 1) and Q-value spectrum (Fig. 2, main text), respectively.

II. DISPERSIVE SPECTRA

We acquired ESR data by monitoring the cavity-sample resonance as the magnetic field was swept. From the resonance peak (absorbed power as a function of frequency f) at each value of field, we extracted values for Q and f_{res} , the system's resonant frequency. The absorption spectra in the main text show Q as a function of H . Dispersive spectra of f_{res} as a function of H allow us to extract similar information about sample-cavity resonance fields. An example of one of these spectra is shown in Supplementary Fig. 1. As expected, a sample-cavity resonance in this spectrum is characterized by an up-down response in f_{res} , centered on the resonance field.

Each peak in an absorption spectrum corresponds to an up-down response in the associated dispersive spectrum. In this example, one can discern five ESR transitions (in order of increasing field): two allowed transitions, followed by a small forbidden transition (marked), then two more allowed transitions.

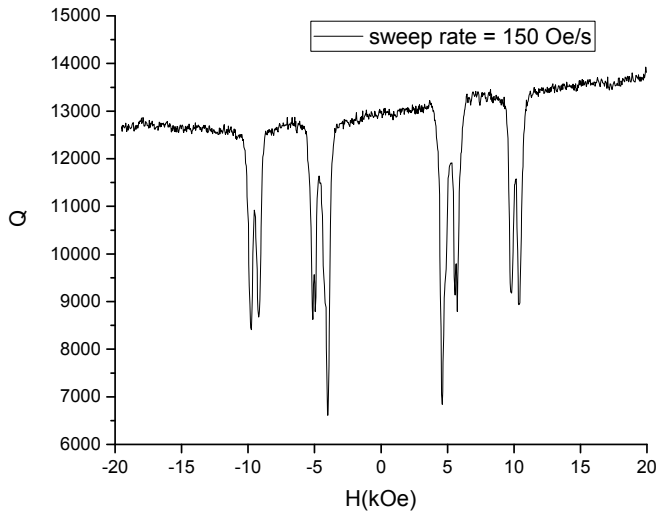


Supplementary Figure 1. Dispersive ESR spectrum for $\theta_H = 31.9^\circ$.

One interesting feature that can be discerned only in the dispersive spectrum is the sign of the f_{res} dependence on field: most ESR transitions show f_{res} to increase initially as the field is increased and then to decrease rapidly when the field passes through the sample-cavity resonance field. This is a result of the Zeeman effect causing levels to move apart as the field is increased. The resonances in Supplementary Fig. 1 at \sim 13 kOe show this typical behavior. These transitions correspond to the right black arrow in Fig. 1 in the main text, where indeed the two levels involved in the transition are moving apart as field increases, i.e., these are levels in the right well in the inset to Fig. 4 (main text). In contrast, the resonances in Supplementary Fig. 1 at \sim 5 kOe have the opposite dispersive behavior, with f_{res} first decreasing with H and then rapidly increasing when resonance is reached. This unusual behavior indicates that the two levels involved in these transitions are moving *closer* to each other as field increases. The left black arrow in Fig. 1 (main text) shows that this transition corresponds to levels exhibiting just that behavior, as they are levels in the left well of Fig. 4 (inset, main text).

III. INDUCTIVE OFFSET CORRECTION

When obtaining our spectra, the magnetic field H is swept at a constant rate of 150 Oe/s. Since the sample chamber and cavity are metallic (mostly copper), the changing field produces an induced magnetic field that opposes dH/dt (Lenz' law). Therefore, the actual H -field applied to the sample is less than the nominal value determined by the current in the magnet coils. To characterize this offset, we took some spectra by sweeping H from -20 kOe to 20 kOe. An example is shown in Supplementary Fig. 2. One can see that the spectrum is not symmetric about $H = 0$, indicating the effect of the induced field. By determining the symmetry point for this spectrum, we found the inductive field offset to be $H_{off} = 301$ Oe. The spectra in Fig. 2 (main text) have been corrected from the raw data by shifting the spectra horizontally (to the left) by H_{off} .



Supplementary Figure 2. ESR spectrum for $\theta_H = 24.2^\circ$ with H swept from -20 kOe to 20 kOe.

IV. CALCULATION OF \vec{B}

Because the ESR spectra were obtained at low applied field and at substantial angles θ_H between the sample's easy (z) axis and \vec{H} , the field experienced by a typical molecule, \vec{B} , is not collinear with \vec{H} . Thus, it is important to carefully transform \vec{H} into \vec{B} in performing our analysis and simulations.

While for any given spectrum θ_H is constant as the field is swept, the angle θ between \vec{B} and the easy axis is changing as H increases because of the spin's anisotropy. To account for this, we diagonalized the Hamiltonian with the \vec{B} along the x, y, and z directions. For each direction, we calculated the magnetization M_i ($i = x, y, z$) as a function of B_i and temperature T using standard statistical mechanical techniques. The molecule's symmetry implies that the susceptibility tensor is diagonal; this becomes only an approximation as H increases.

We then used the relations

$$H_i = B_i - 4\pi\alpha M_i(B_i, T), \quad (1)$$

where α is a parameter on the order of unity that takes into account lattice-structure and crystal-shape (demagnetization) effects and is treated as a free parameter. For a given θ_H , we calculate H_i using:

$$\begin{aligned} H_z &= H \cos(\theta_H) \\ H_x &= H \sin(\theta_H) \cos(\phi_H) \\ H_y &= H \sin(\theta_H) \sin(\phi_H), \end{aligned} \quad (2)$$

where ϕ_H is the angle of the transverse component of H with respect to the hard (x) axis and, in practice, has a very small effect. Using Eq. 2 and numerically inverting Eq. 1, we can calculate $B_i(H, \theta_H, \phi_H, T)$ and thereby calculate $B = |\vec{B}|$ and $\theta = \arccos(B_z/B)$, which are the values plotted in Fig. 3 (main text). In simulating the spectra, B and θ vary as a function of H for fixed θ_H . Through the fitting procedure described below, we determined best-fit values of α and θ_H . We treated α as a single parameter (with best-fit value of 0.323(3)) that is independent of θ_H . The spectrum labels in Fig. 2 (main text) are the values of θ_H determined from optimization.

V. FITTING OF SPECTRAL PEAKS

Spectra could readily be simulated using the EasySpin package.¹ However, fitting of the experimental spectra are complicated by the fact that the forbidden transitions are typically very small compared with allowed transitions. Therefore, a least-squares minimization procedure that compares experimental and simulated spectra effectively ignores forbidden-transition peaks for most values of θ_H . Instead, we adopted a different fitting procedure that treats all observed peaks with equal weight. By fitting the experimental spectral peaks to Lorentzian functions, we determined the field position, $B_{data,i}$, and area, $I_{data,i}$, for the i th peak. A least-squares fitting method was then applied to determine the anisotropy parameters for both components and α , as well as the angles θ_H . The χ^2 for each peak is defined as:

$$\chi_i^2(\theta_H) = \left(\frac{B_{sim,i}(\theta_H) - B_{data,i}}{\Delta B_{data,i}} \right)^2 + \left(\frac{I_{sim,i}(\theta_H) - I_{data,i}}{\Delta I_{data,i}} \right)^2 \quad (3)$$

where $\Delta B_{data,i}$ and $\Delta I_{data,i}$ are the uncertainties in $B_{data,i}$ and $I_{data,i}$, respectively, as determined from the Lorentzian peak fitting. $B_{sim,i}(\theta_H)$ and $I_{sim,i}(\theta_H)$ are the values determined from simulations of the corresponding peaks for given anisotropy parameters and α and θ_H . For the + forbidden transitions, the peaks from the two components overlapped for many values of θ_H . So, in calculating χ^2 for those peaks, we included the mean position and the total area of the peaks.

The total χ^2 was calculated by summing over all the peaks from all spectra:

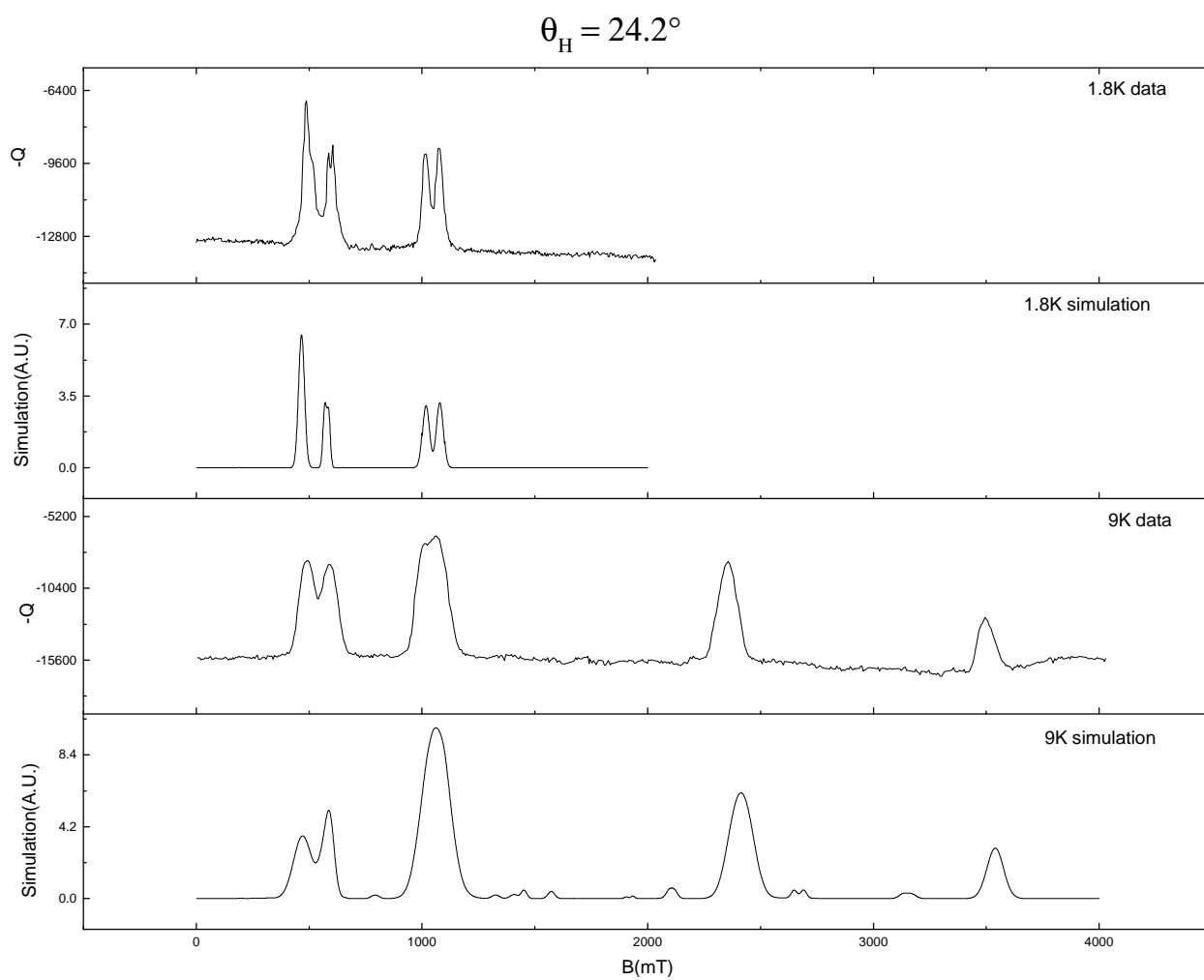
$$\chi_{total}^2 = \sum_i \sum_{\theta_H} \chi_i^2(\theta_H) \quad (4)$$

χ_{total}^2 was minimized to give the optimized values of anisotropy parameters and α as well as all values of θ_H . Anisotropy parameters and α were taken to be the same for all peaks from all spectra. Peaks from the same spectra were forced to have the same value of θ_H . The resulting fitting parameters were then used to further correct the calculated values of M_i , as described in the preceding section. The above procedure was then iterated until it converged.

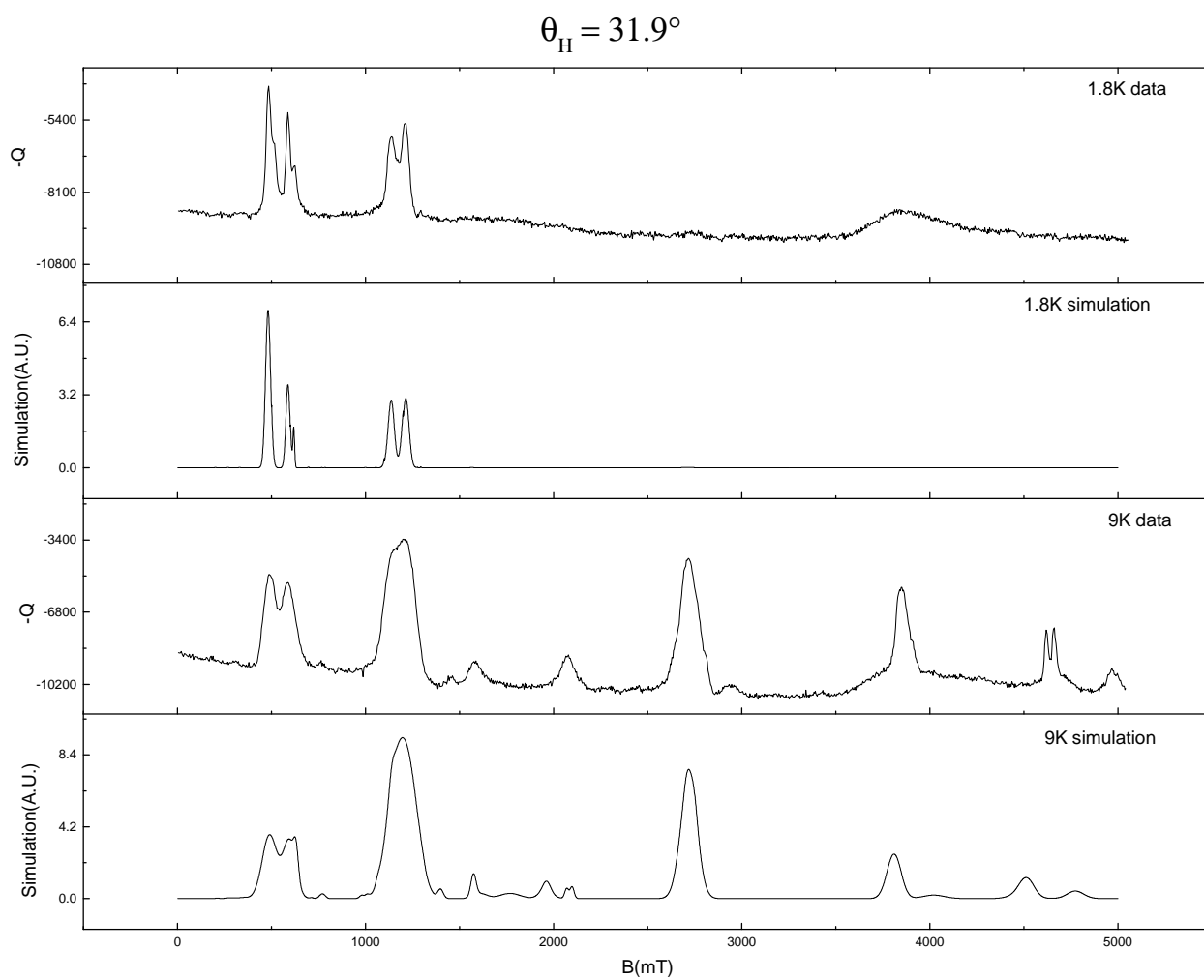
This fitting procedure was applied only to data obtained at

1.8 K. An important check of the validity of the fit is to compare experimental and simulated spectra at higher temperatures that involve transitions between high-lying excited states that are unobservable at 1.8 K. We compared our experimental and simulated spectra at several temperatures studied (see Supplementary Figs. 3–13 for a comparison at 1.8 and 9 K). The comparisons show that the simulations reproduce the experimental data well. Since our fitting procedure involves only peak positions and areas, the peak width was manually adjusted in these simulations (parameter HStrain in EasySpin) to achieve reasonable agreement. As can be seen in the figures, the width at 9 K is roughly a factor of three larger than at 1.8 K.

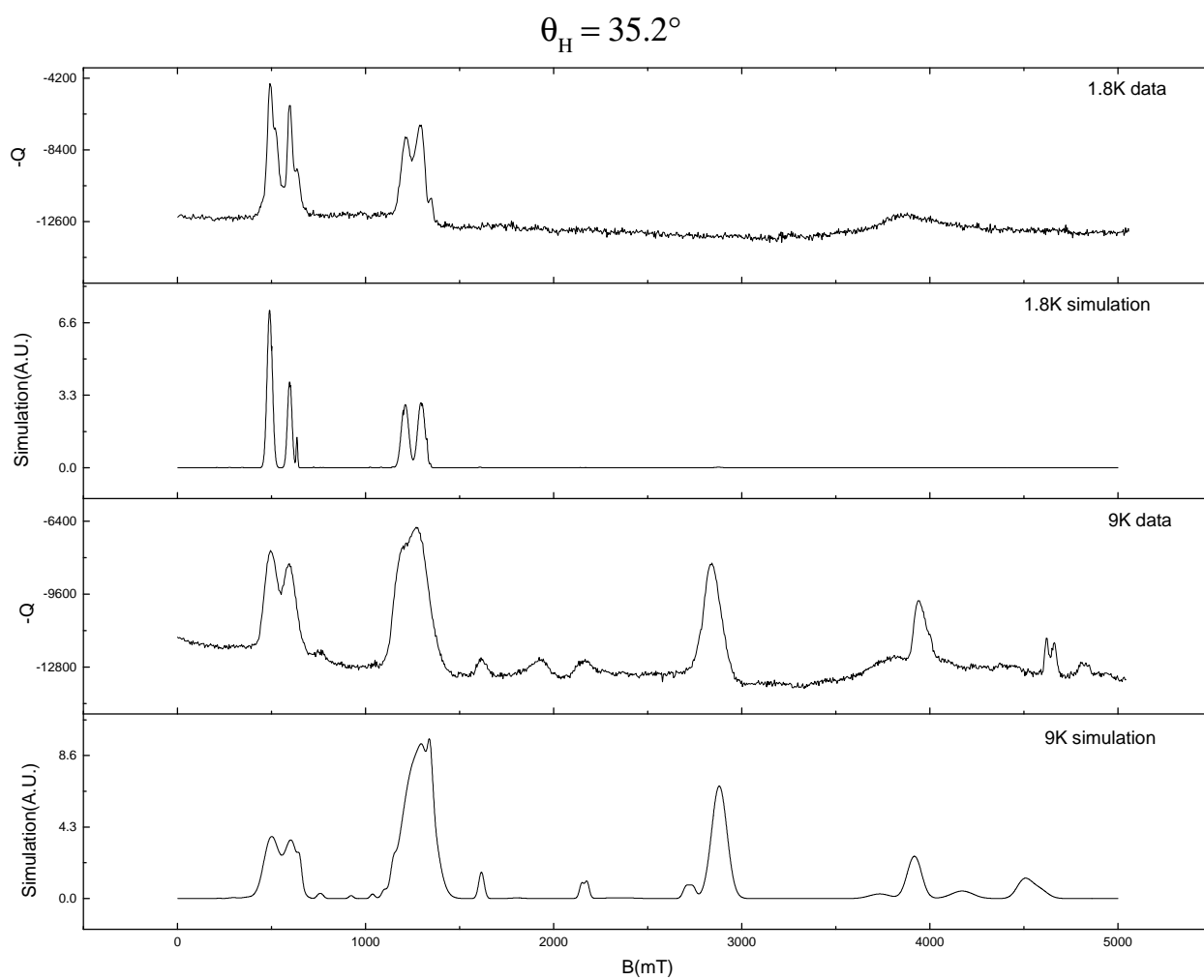
¹ S. Stoll and A. Schweiger, *Journal of Magnetic Resonance* **178**, 42 (2006).



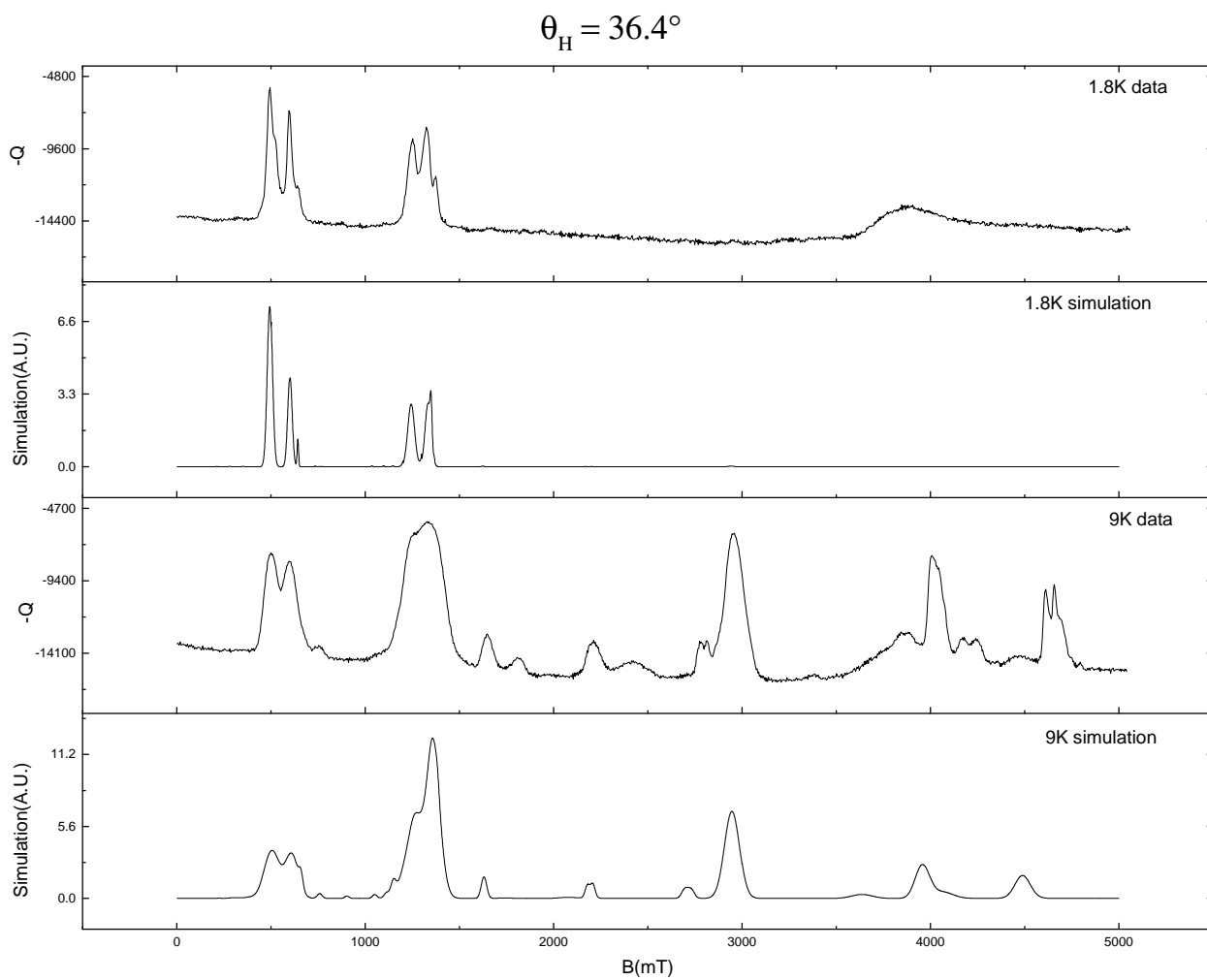
Supplementary Figure 3. Comparison of experimental and simulated spectra at 1.8 and 9 K, as indicated for $\theta_H = 24.2^\circ$.



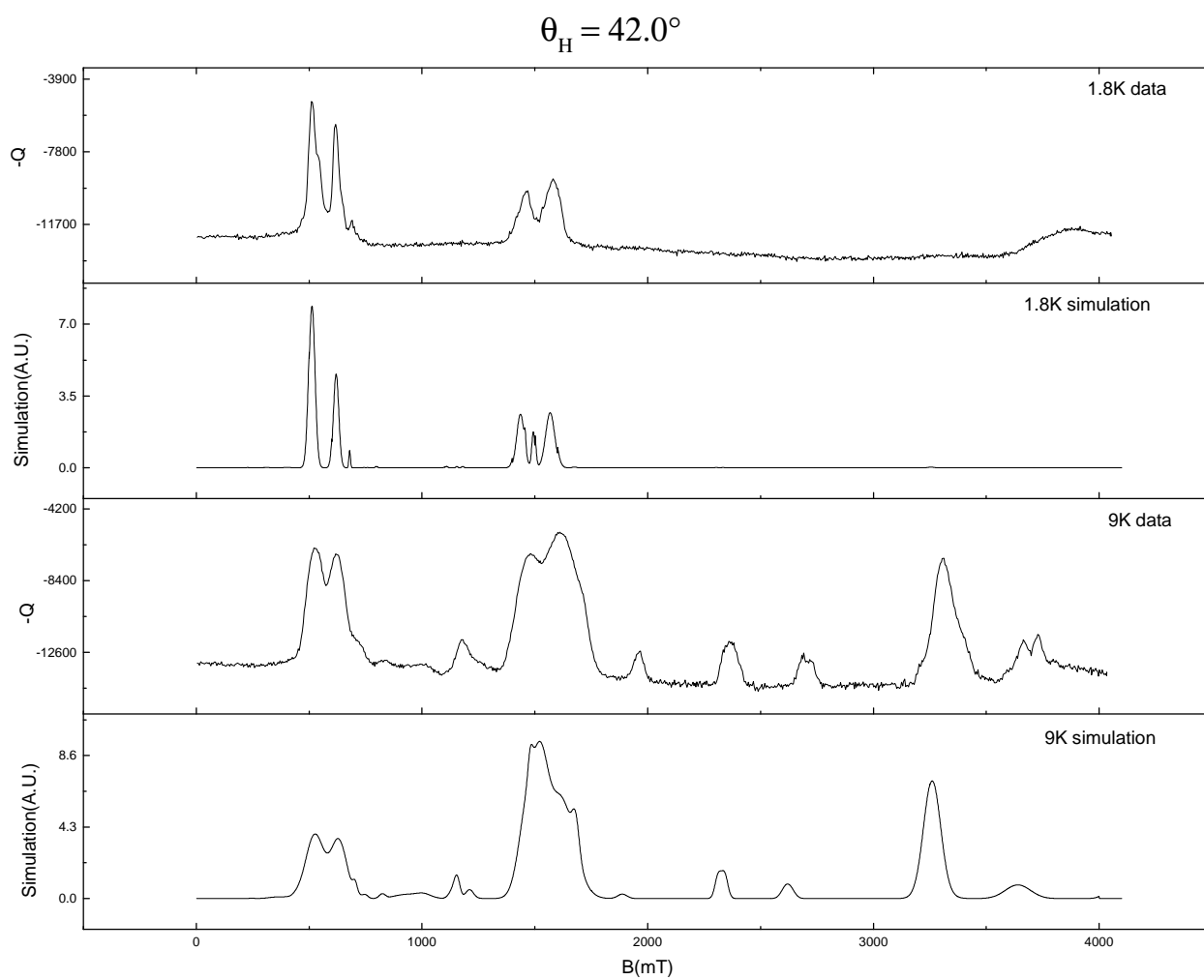
Supplementary Figure 4. Comparison of experimental and simulated spectra at 1.8 and 9 K, as indicated for $\theta_H = 31.9^\circ$.



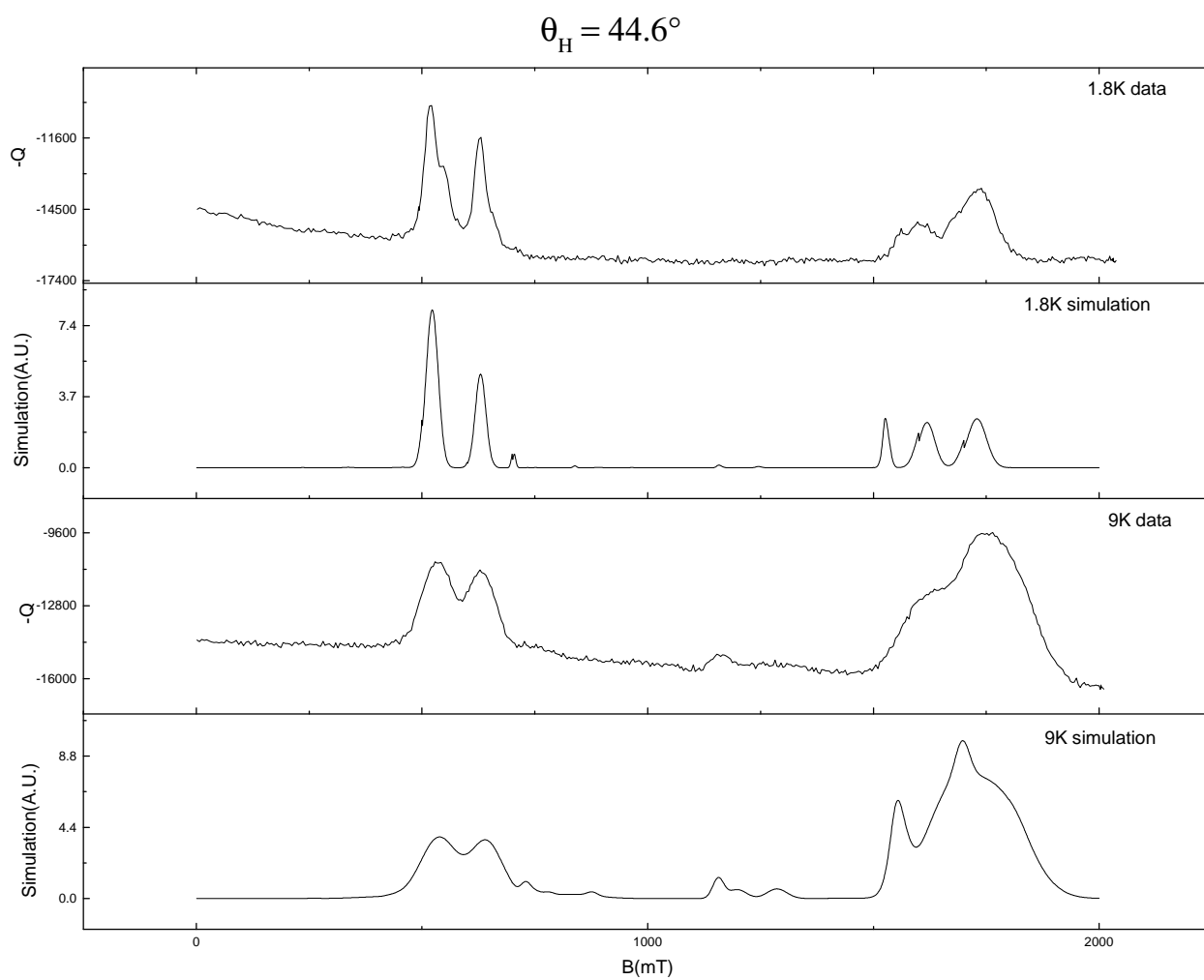
Supplementary Figure 5. Comparison of experimental and simulated spectra at 1.8 and 9 K, as indicated for $\theta_H = 35.2^\circ$.



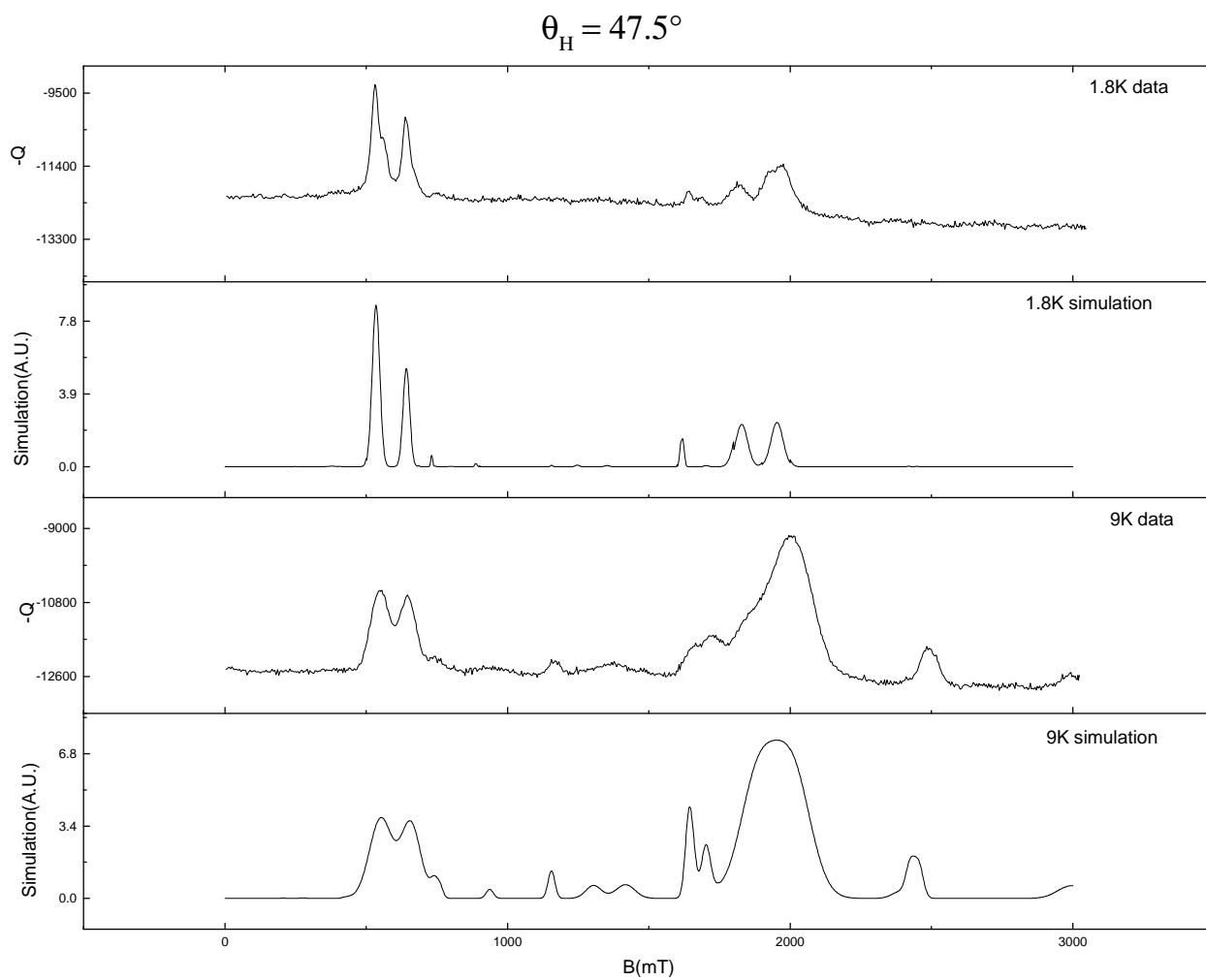
Supplementary Figure 6. Comparison of experimental and simulated spectra at 1.8 and 9 K, as indicated for $\theta_H = 36.4^\circ$.



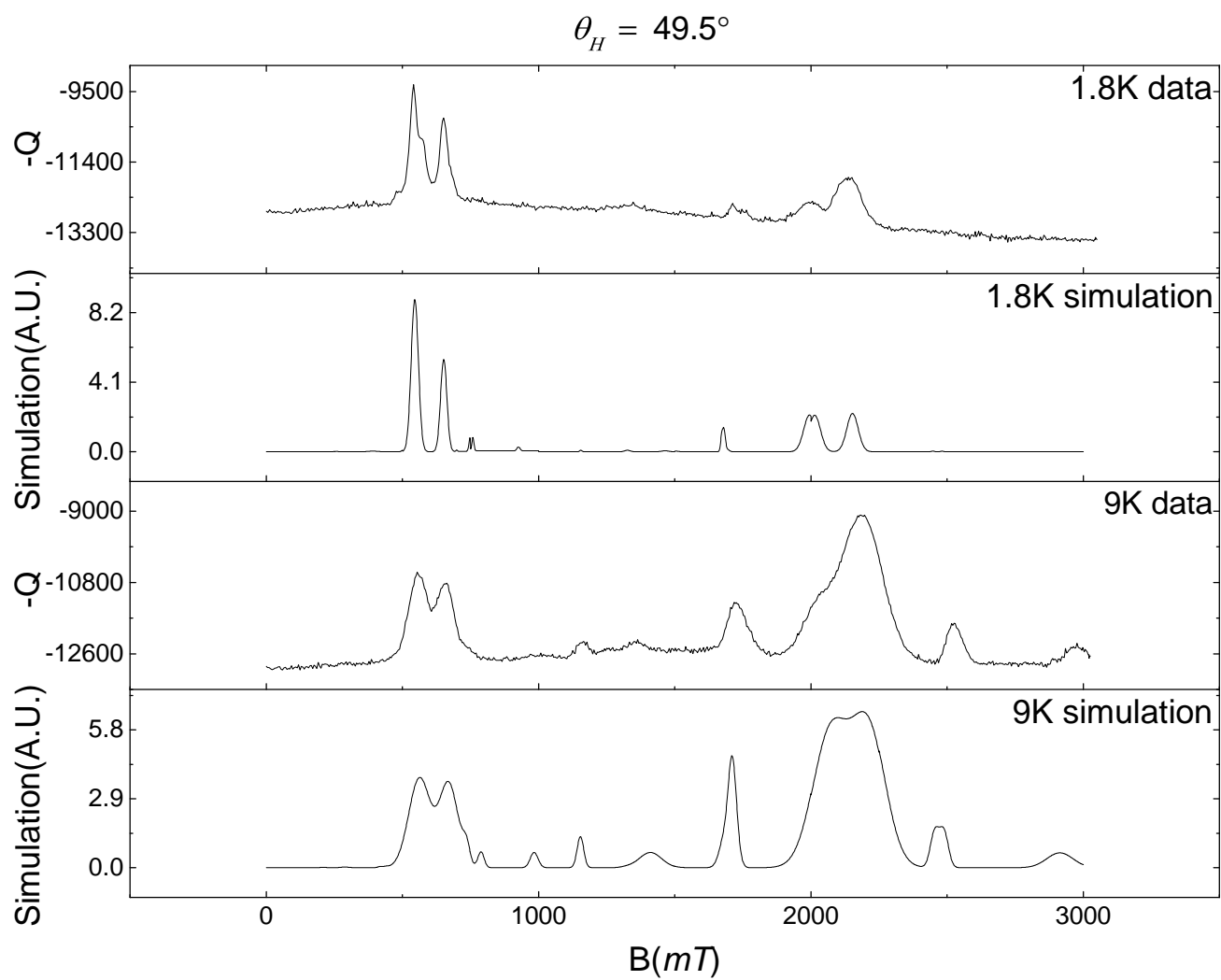
Supplementary Figure 7. Comparison of experimental and simulated spectra at 1.8 and 9 K, as indicated for $\theta_H = 42.0^\circ$.



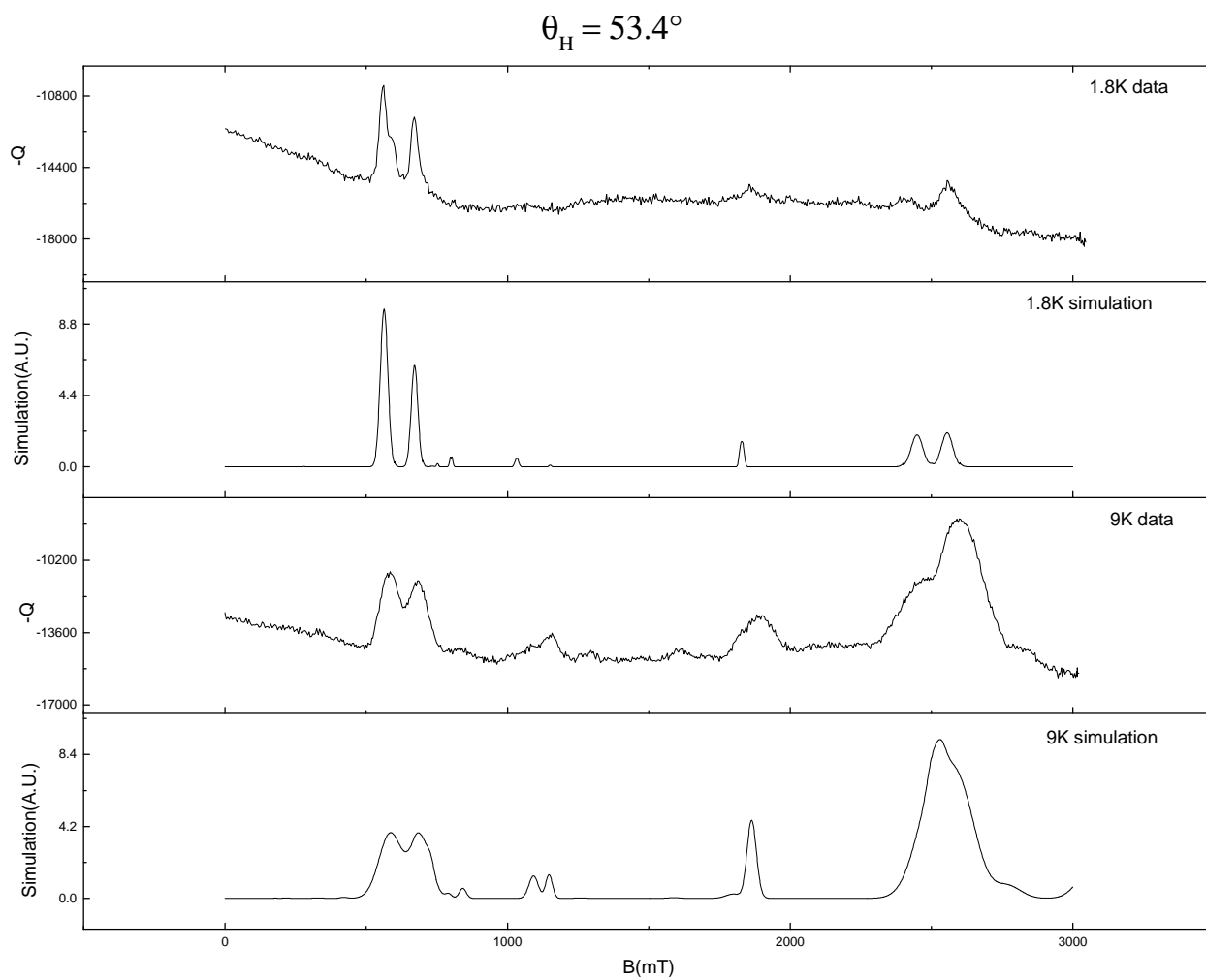
Supplementary Figure 8. Comparison of experimental and simulated spectra at 1.8 and 9 K, as indicated for $\theta_H = 44.6^\circ$.



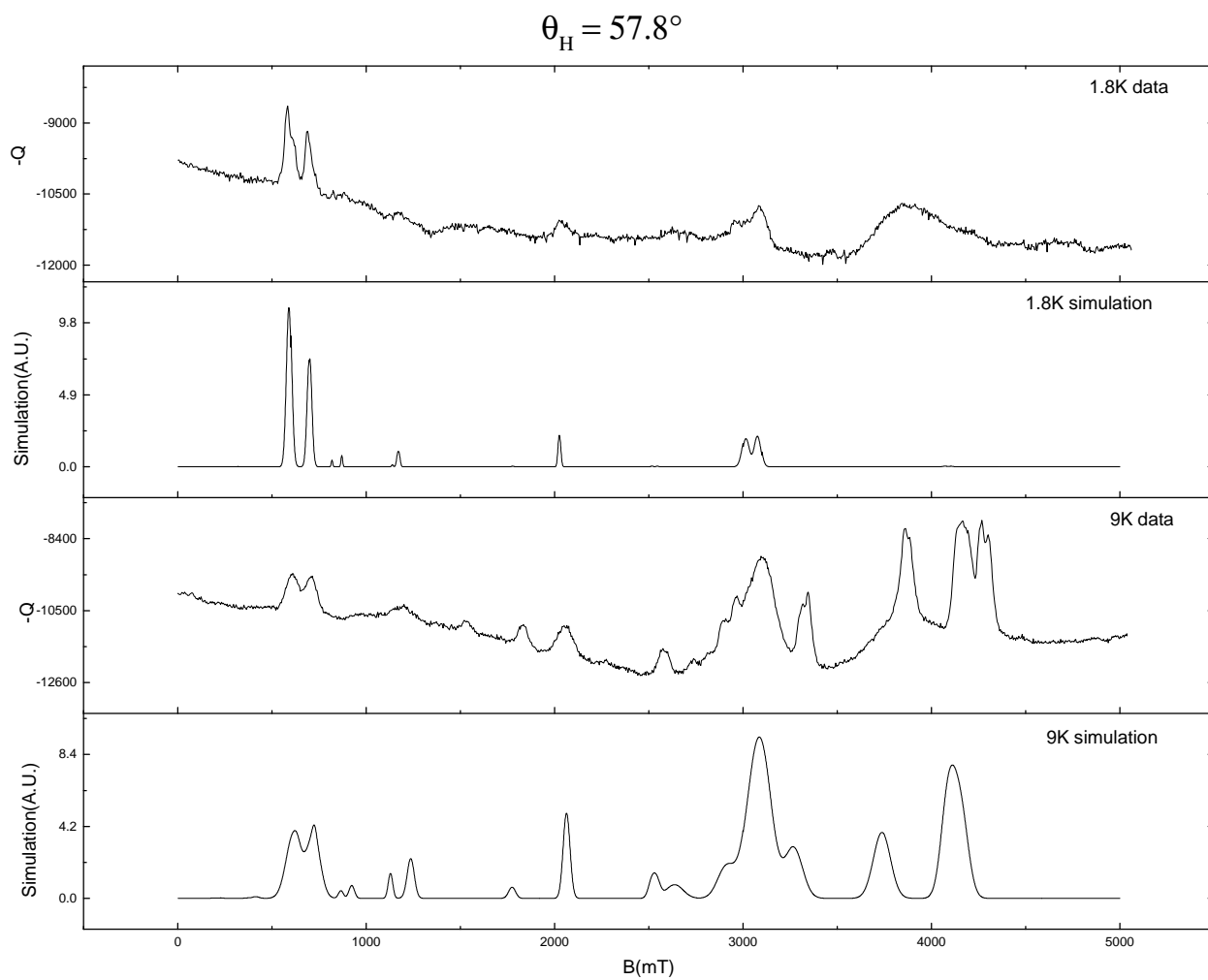
Supplementary Figure 9. Comparison of experimental and simulated spectra at 1.8 and 9 K, as indicated for $\theta_H = 47.5^\circ$.



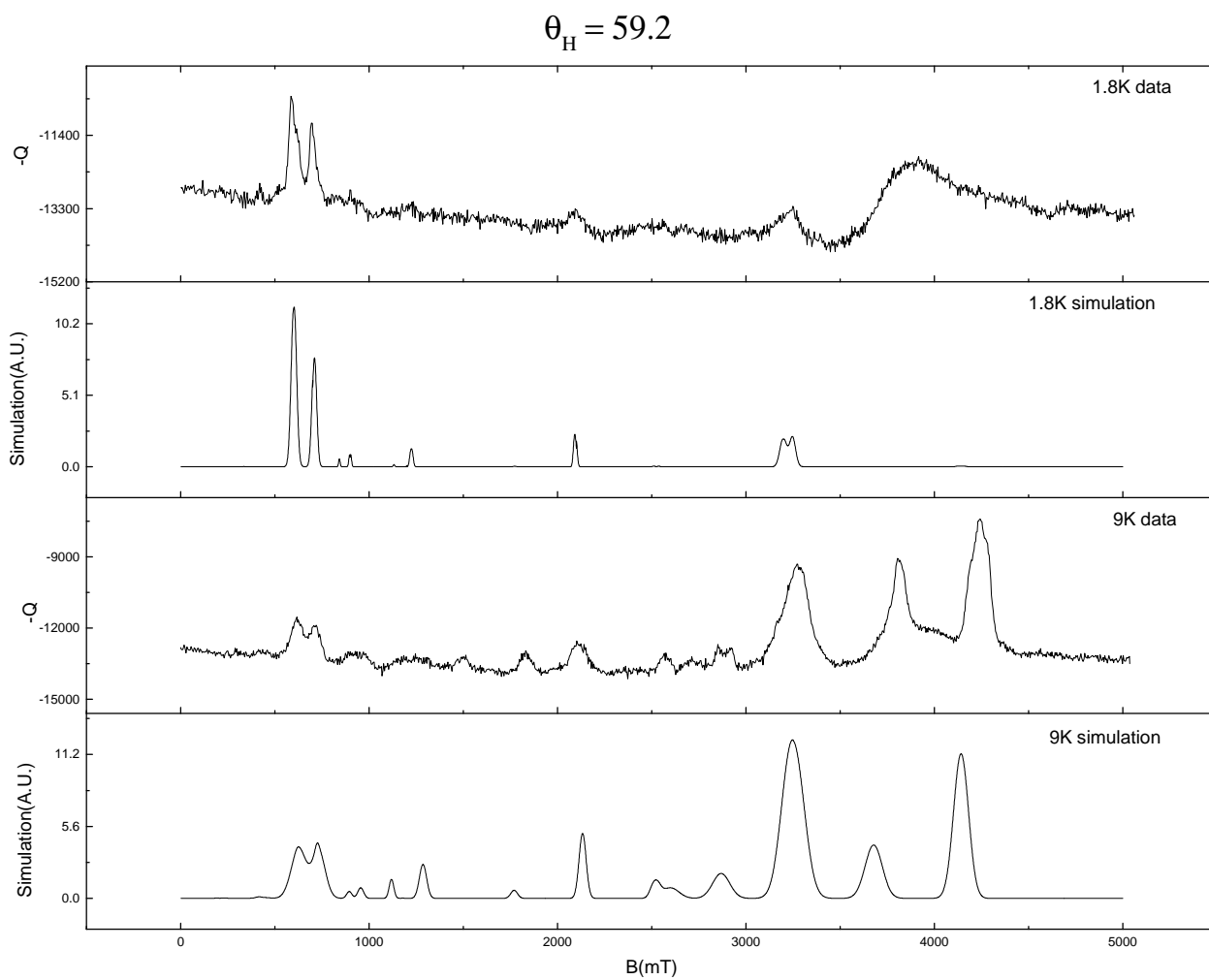
Supplementary Figure 10. Comparison of experimental and simulated spectra at 1.8 and 9 K, as indicated for $\theta_H = 49.4^\circ$.



Supplementary Figure 11. Comparison of experimental and simulated spectra at 1.8 and 9 K, as indicated for $\theta_H = 53.4^\circ$.



Supplementary Figure 12. Comparison of experimental and simulated spectra at 1.8 and 9 K, as indicated for $\theta_H = 57.8^\circ$.



Supplementary Figure 13. Comparison of experimental and simulated spectra at 1.8 and 9 K, as indicated for $\theta_H = 59.2^\circ$.